

# Design of an Underactuated Peristaltic Robot on Soft Terrain

Scott Scheraga<sup>†</sup>, Alireza Mohammadi<sup>‡</sup>, Taehyung Kim<sup>‡</sup>, and Stanley Baek<sup>††</sup>

**Abstract**—This paper presents an innovative robotic mechanism for generating peristaltic motion for robotic locomotion systems. The designed underactuated peristaltic robot utilizes a minimum amount of electromechanical hardware. Such a minimal electromechanical design not only reduces the number of potential failure modes but also provides the robot design with great potential for scaling to larger and smaller applications. We performed several speed and force generation tests atop a variety of granular media. Our experiments show the effective design of robot mechanism where the robot can travel with a small input power (1.14W) at 6.0 mm/sec with 2.45 N force atop sand.

## I. INTRODUCTION

Over the past decade, researchers have investigated bio-inspired robots for usage in narrow soft-terrain and fluidic environments across a variety of applications such as tunneling during space exploration missions [1], gastrointestinal endoscopy [2], and underwater exploration [3], [4]. Bio-inspired robots that are designed for such operations often utilize complex actuators where their electromechanical complexity may lead to a multitude of failure modes.

Peristalsis occurs when waves of alternating contraction and relaxation of longitudinal and/or oblique muscles move along the length of a radially flexible tube [5]. In earthworms, longitudinal and circumferential muscles alternate contraction periods, to produce local areas of larger diameter. Bio-inspired robots that perform inchworm-type locomotion utilize their body segments in a way to alternate between phases of anchoring to their environment, and phases of retracted-anchor advancement [6], [7]. Another type of bio-inspired inchworm-type actuation method involves peristalsis of the outer surface of the robot, whereby at least three body segments operate in alternating phases of anchoring and propulsion [1]. As illustrated in Fig. 1, peristaltically-actuated organisms generally traverse their terrain in a direction that is opposite to the direction of the contractive traveling waves, which propagate through their bodies.

Despite the prevalence of peristaltic locomotion in nature, which is observed in organisms such as earthworms, eel

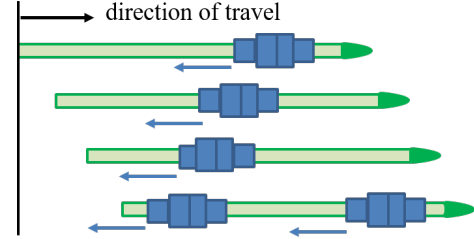


Fig. 1: Retrograde contraction wave (blue arrows) that underlies bio-inspired peristaltic locomotion.

worms, leaches, amoebas, boas, and vipers [8]–[10], peristalsis is an under-utilized robotic propulsion method. Existing peristaltic or inchworm robots tend to have a high degree of electromechanical complexity. Indeed, these complex mechanisms often require multiple independently controlled actuators in order to contract the robot body segments longitudinally as well as circumferentially. Examples of these independent actuation mechanisms include but are not limited to the lead-screw pantograph-type mechanisms [1], lead-screw-actuated segments [2], servo-crank mechanisms [11], motor-driven radial anchors and longitudinal extenders in robotic inchworms [6], which are used for biomedical applications, and the ionic polymer-metal composites [12].

The use of a single motor and cylindrical cam would make it much easier to scale the robot to larger or smaller sizes. Furthermore, a robotic mechanism design, which relies on a single motor for achieving propulsion, would reduce the mechanical complexity of the robot in comparison with other peristaltic mechanisms that involve multiple linear actuators or tension cables making them prone to more failure modes. The aforementioned concept of a robotic platform actuated by a cylindrical cam-driven propulsive mechanism was investigated by Boxerbaum *et al.* [13], where the proposed mechanism utilizes a cam/crank that drives contractive waves through interwoven steel cables.

Using a Sarrus linkage topology and inspired by the dual-pantograph propulsion units proposed by Omori *et al.* [1], we have designed a single-motor peristaltic mechanism for robotic propulsion on soft or granular terrain. The proposed mechanism is designed in a way that the motion of the legs are entirely coordinated by the movement of cam-followers on phase-shifted sinusoidal profiles that are grooved on the cam as shown in Fig. 2 (b). Since our mechanism is not dependent on any spring-loaded elements, movement halts of the robot due to media packing issues underneath the legs are avoided to a large extent. Through experiments on

\*Distribution A. Appeared for Public Release: Distribution Unlimited. The views expressed in this article are those of authors and not necessarily those of the U.S. Air Force Academy, the U.S. Air Force, the Department of Defense, or the U.S. Government. PA#: USAFA-DF-2019-429

<sup>†</sup>S. Scheraga is with the Department of Mechanical Engineering, University of Colorado, Boulder, CO 80309, USA

<sup>‡</sup>A. Mohammadi and T. Kim are with the Department of Electrical and Computer Engineering, University of Michigan-Dearborn, Dearborn, MI 48128, USA

<sup>††</sup>S. Baek is with the Department of Electrical and Computer Engineering, United States Air Force Academy, USAF Academy, CO 80840, USA

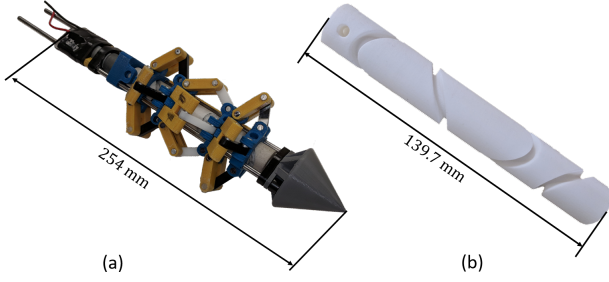


Fig. 2: (a) Peristaltic robotic platform with body frame-static nosecone (b) 3D printed cylindrical cam with phase-shifted sinusoidal grooves.

various terrain profiles, we demonstrate that our propulsive mechanism is capable of reliable surface travel in granular media across a wide range of angles of repose. Furthermore, we present a dynamical model for peristaltic locomotion which captures the propulsive effect of phase shifts between the engraved grooves on the rotating axial-cam.

The rest of this paper is organized as follows. In Section II, we present a dynamic model for peristaltic locomotion and demonstrate how proper phase shifts between the engraved grooves on the axial-cam would induce forward propulsion while the cam is rotating. Next, in Section III, we present our constructed robotic mechanism along with the design details for the cylindrical cam, the passive legs, and the cam-followers. Thereafter, in Section IV, we present the capabilities of our robot in traversing granular media through several experiments. Finally, we conclude the paper with some final remarks and future research directions in Section V.

## II. DYNAMIC MODELING OF PERISTALTIC LOCOMOTION

In this section, we present a dynamic model for peristaltic locomotion and demonstrate how proper phase shifts between the engraved grooves on the axial-cam would induce forward propulsion while the cam is rotating. As it will be shown later, the presented model effectively captures the propulsive effect of the phase-shifted sinusoidal layout on the grooved cam.

Our modeling approach is inspired by the multi-block model by Tanaka *et al.* [8], where the peristalsis-like locomotion is modeled by elongation-contraction waves that propagate along the body axes of the insects that perform peristaltic locomotion. We remark that a similar modeling approach has been used in snake robotics literature [14], [15] to control snake robot locomotion using a simplified prismatic joint model of planar snake robots. In this work, we are using the notation by Liljebäck *et al.* [15].

The block diagram of the dynamic system, which models the propulsive locomotion of the robotic mechanism, is depicted in Fig. 3. As it can be seen from Fig. 3, the robotic mechanism is modeled by a collection of  $N$  inter-connected links that are subject to ground friction forces. Furthermore, each link, with the exception of the first and the last links, is connected to two other links via two springs. The springs

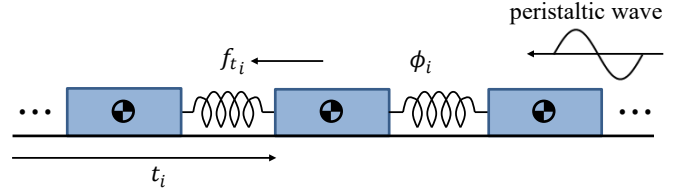


Fig. 3: Dynamic modeling of peristaltic locomotion.

capture the effect of peristalsis-like driving forces in the robotic mechanism.

We denote the horizontal position of the center of mass of the  $i^{\text{th}}$  link, where  $1 \leq i \leq N$ , by  $t_i$  and the length of the spring connecting the  $i^{\text{th}}$  and  $i+1^{\text{th}}$  links by  $\phi_i$ . Therefore, we have

$$\phi_i - t_{i+1} + t_i = 0, \quad 1 \leq i \leq N-1. \quad (1)$$

Denoting the vector of link positions and spring lengths by  $\mathbf{t} = [t_1, \dots, t_N]^T \in \mathbb{R}^N$  and  $\boldsymbol{\phi} = [\phi_1, \dots, \phi_{N-1}]^T \in \mathbb{R}^{N-1}$ , respectively, the equation in (1) can be written in the following vector format

$$\mathbf{D}\mathbf{t} + \boldsymbol{\phi} = \mathbf{0}, \quad (2)$$

where

$$\mathbf{D} = \begin{bmatrix} 1 & -1 & 0 & \cdots & 0 \\ 0 & 1 & -1 & \cdots & 0 \\ & & \ddots & \ddots & \\ 0 & \cdots & 0 & 1 & -1 \end{bmatrix} \in \mathbb{R}^{(N-1) \times N}. \quad (3)$$

Furthermore, the position of the center of mass of the mechanism is given by

$$p_x = \frac{1}{N} \mathbf{e}^T \mathbf{t}, \quad (4)$$

where  $\mathbf{e} = [1 \ \cdots \ 1]^T \in \mathbb{R}^N$ . Since  $\text{rank}(\mathbf{D}) = N-1$ , it has a right inverse, which is given by  $\bar{\mathbf{D}} = \mathbf{D}^T (\mathbf{D}\mathbf{D}^T)^{-1}$ . Concatenating (2) and (4), we have

$$\begin{bmatrix} \mathbf{D} \\ \frac{1}{N} \mathbf{e}^T \end{bmatrix} \mathbf{t} = \begin{bmatrix} -\boldsymbol{\phi} \\ p_x \end{bmatrix}. \quad (5)$$

Solving (5) for  $\mathbf{t}$ , we obtain

$$\mathbf{t} = \mathbf{e} p_x - \bar{\mathbf{D}} \boldsymbol{\phi}, \quad (6)$$

from which it immediately follows that

$$\dot{\mathbf{t}} = \mathbf{e} \dot{p}_x - \bar{\mathbf{D}} \dot{\boldsymbol{\phi}}. \quad (7)$$

Equation (7) captures the kinematic relationship between the absolute velocities of the robot body segments and the rate of change of relative distances between these segments.

In order to derive the dynamical equations of motion of our peristaltic mechanism, we model the total force on the  $i^{\text{th}}$  link by a combination of viscous ground friction forces and linear spring-like forces, which capture the effect of the underlying propulsive forces of the peristaltic actuation mechanism. In particular, we model the force on the  $i^{\text{th}}$  link by

$$f_{t_i} = -c_1 \dot{t}_i + c_2 (\dot{\phi}_i + \dot{\phi}_{i-1}), \quad 2 \leq i \leq N-1, \quad (8)$$

where  $c_1$  is the viscous ground friction coefficient and  $c_2$  is the spring coefficient of the propulsive peristaltic force acting on the  $i^{\text{th}}$  link. For the first and the last links, which are merely connected to one adjacent link, we have

$$f_{t_1} = -c_1 \dot{t}_1 + c_2 \phi_1, f_{t_N} = -c_1 \dot{t}_N + c_2 \phi_{N-1}. \quad (9)$$

Using the adopted notation in Nomenclature, the equations in (8) and (9) can be written in the following succinct format

$$\mathbf{f}_t = -c_1 \dot{\mathbf{t}} + c_2 \text{diag}(\mathbf{A}^\top \boldsymbol{\phi}) \mathbf{e}, \quad (10)$$

where

$$\mathbf{A} = \begin{bmatrix} 1 & 1 & 0 & \cdots & 0 \\ 0 & 1 & 1 & \cdots & 0 \\ & & \ddots & \ddots & \\ 0 & \cdots & 0 & 1 & 1 \end{bmatrix} \in \mathbb{R}^{(N-1) \times N}. \quad (11)$$

and  $\text{diag}(\cdot)$  is an operator that produces a diagonal matrix with the elements of its argument along its diagonal.

Summing the equations given by (8) and (9), which is equivalent to multiplying both sides of (10) by  $\mathbf{e}^\top$ , yields

$$f_t = -c_1 \mathbf{e}^\top \dot{\mathbf{t}} + c_2 \mathbf{e}^\top \text{diag}(\mathbf{A}^\top \boldsymbol{\phi}) \mathbf{e}. \quad (12)$$

Subsequently, using the relation given by (7) and (12), we have

$$f_t = -c_1 \mathbf{e}^\top \mathbf{e} \dot{p}_x + c_1 \mathbf{e}^\top \overline{\mathbf{D}} \dot{\boldsymbol{\phi}} + c_2 \mathbf{e}^\top \text{diag}(\mathbf{A}^\top \boldsymbol{\phi}) \mathbf{e}. \quad (13)$$

Noting that  $\mathbf{e}^\top \mathbf{e} = N$ ,  $\mathbf{e}^\top \text{diag}(\mathbf{A}^\top \boldsymbol{\phi}) \mathbf{e} = 2\bar{\mathbf{e}}^\top \boldsymbol{\phi}$ , and  $\mathbf{e}^\top \overline{\mathbf{D}} = 0$ , we can write

$$f_t = -c_1 N \dot{p}_x + 2c_2 \bar{\mathbf{e}}^\top \boldsymbol{\phi}. \quad (14)$$

Finally, denoting the total inertia of the robotic mechanism by  $m$  and noting that  $m\ddot{p}_x = f_t$ , we arrive at

$$\ddot{p}_x = -\frac{c_1 N}{m} \dot{p}_x + \frac{2c_2}{m} \bar{\mathbf{e}}^\top \boldsymbol{\phi}. \quad (15)$$

Therefore, the final dynamical model of the peristaltic robotic mechanism can be written as

$$\ddot{p}_x + \alpha_1 \dot{p}_x = \alpha_2 \bar{\mathbf{e}}^\top \boldsymbol{\phi}, \quad (16)$$

where

$$\alpha_1 = \frac{c_1 N}{m} \text{ and } \alpha_2 = \frac{2c_2}{m}.$$

**Remark 1.** The dynamic model in (16) represents a first order linear time invariant (LTI) system, which is being driven by the input  $\boldsymbol{\phi}$ . The input  $\boldsymbol{\phi}$  is determined by the phase-shifted sinusoidal profiles that are grooved on the cylindrical cam and the frequency of rotation of the cam about its axis.

**Remark 2.** The dynamic model in (16) has only two parameters  $\alpha_1$  and  $\alpha_2$ , which lump the effect of the viscous ground friction forces and the underlying driving peristaltic force that causes forward propulsion. These two unknown parameters can be easily identified by performing tests as outlined in Section IV.

**Remark 3.** The dynamic model in (16) only captures the propulsion peristaltic force. Including the effect of the rota-

tional slipping forces that cause non-straight displacements is the subject of a future work.

In order to analyze the effect of phase shifts between the grooves on the cylindrical cam, we consider the input function  $\boldsymbol{\phi}$  in the dynamic model given by (16). The input function  $\boldsymbol{\phi}$  is determined by the grooved sinusoidal layout and the frequency of rotation of the cylindrical cam. In particular, the input function  $\boldsymbol{\phi}$  is given by  $\boldsymbol{\phi}_c(t, \boldsymbol{\delta})$  (see the Nomenclature), where

$$\boldsymbol{\phi}_c(t, \boldsymbol{\delta}) = k \begin{bmatrix} \cos(\omega t) \\ \cos(\omega t - \delta_1) \\ \vdots \\ \cos(\omega t - \delta_{N-2}) \end{bmatrix} \in \mathbb{R}^{N-1}. \quad (17)$$

In Equation (17),  $\omega$  and  $k$  denote the frequency of rotation of the cam and the amplitude of the sinusoidal grooves, respectively. Furthermore, the vector of phase shifts is given by  $\boldsymbol{\delta} = [\delta_1 \ \delta_2 \ \cdots \ \delta_{N-2}]^\top \in \mathbb{R}^{N-2}$ .

Integrating both sides of the dynamic model in (16) and assuming that  $p_x(0) = 0$  and  $\dot{p}_x(0) = 0$ , we get

$$\dot{p}_x + \alpha_1 p_x = \frac{\alpha_2}{\omega} \bar{\mathbf{e}}^\top \boldsymbol{\phi}_s(t, \boldsymbol{\delta}) + \frac{k\alpha_2}{\omega} \sum_{i=1}^{N-2} \sin(\delta_i), \quad (18)$$

where

$$\boldsymbol{\phi}_s(t, \boldsymbol{\delta}) = k \begin{bmatrix} \sin(\omega t) \\ \sin(\omega t - \delta_1) \\ \vdots \\ \sin(\omega t - \delta_{N-2}) \end{bmatrix} \in \mathbb{R}^{N-1}. \quad (19)$$

As it can be seen from (18), the constant input  $\frac{k\alpha_2}{\omega} \sum_{i=1}^{N-2} \sin(\delta_i)$ , which depends on the phase shifts of the sinusoidal grooves, is what causes propulsion during the peristaltic locomotion.

Figure 4 depicts the numerical simulation results of displacement over time of a peristaltic robotic mechanism, whose dynamics are governed by (16). As it can be seen from Fig. 4, changing the direction of rotation of the axial cam would induce motion in an opposite direction. The inset in Fig. 4 from the same numerical simulation depicts the mechanism displacement over time during one cam rotation, which corresponds to the blue curve bounded by the green box. As it can be seen in the inset in Fig. 4, our derived dynamic model in this section captures the backsliding phenomenon that is observed in peristaltic locomotion. In Section IV, it will be shown that the experimental results obtained from our constructed robotic mechanism have a very close resemblance to the numerical simulation studies associated with the derived dynamical model.

### III. DESIGN OF THE PERISTALTIC ROBOTIC MECHANISM

In this section, we present the design and structure of our peristaltic robotic mechanism, whose exploded view is demonstrated in Fig. 5. First, we present the design details of the cylindrical cam as well as the geometry of the passive legs of the robot. Next, we describe the underlying operation of the cam-followers.

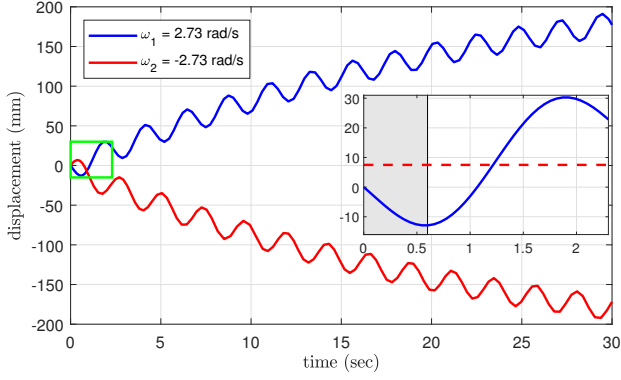


Fig. 4: Numerically simulated time profiles of the displacement of the mechanism in two numerical simulations. The blue and the red curves correspond to the clockwise and the counterclockwise rotations of the cylindrical cam, respectively. One period of the cam rotation bounded by the green box is plotted in the inset. The segment of the locomotion stride in which the mechanism backslides is indicated via the gray background. The dashed red line corresponds to the average displacement ( $\approx 7.5$  mm) of the center of mass of the mechanism in one stride.

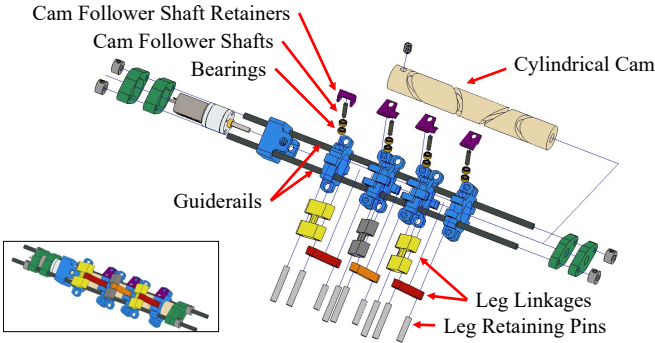


Fig. 5: Exploded view of the peristaltic robot platform, with only one row of leg linkages displayed for visual clarity.

#### A. Cylindrical Cam Design and Passive Leg Geometry

The principal idea behind our peristaltic robotic mechanism, which is depicted in Fig. 2, is based on coordinating the motion of a collection of passive leg linkages, which move according to a contractive-expansive motion pattern, by rotating a cylindrical cam with phase-shifted sinusoidal grooves on it. Our leg linkage design is based on the concept of classical Sarrus linkages [16], and was inspired from the dual-pantograph propulsion units in [1].

**Remark 3.** Our proposed leg linkage geometry, which is depicted in Fig. 6, aims to avoid the halting problems, which are associated with granular media getting packed underneath the leg of the robotic mechanism. If the leg linkage geometry is not designed properly, the halting problems get exacerbated once the legs are covered by a protective sheath.

In order to achieve alternating periods of contraction and expansion in the robotic platform, we use a rotating cylindrical cam, which is depicted in Fig. 2 (b). The rotating cylindrical cam is used to coordinate the motion of the body

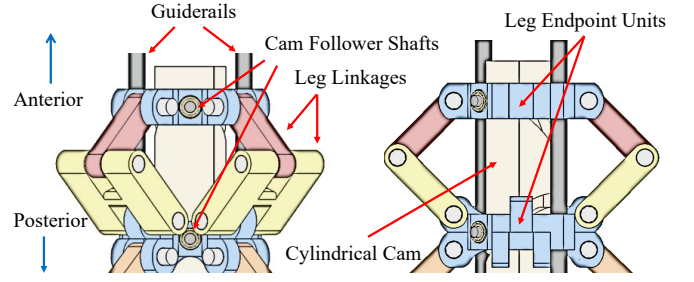


Fig. 6: CAD model side views of a single body segment with component nomenclature. The right-side image is axially rotated  $45^\circ$ , with one set of leg linkages removed.

segments of the robotic platform shown in Fig. 6. Each body segment consists of a pair of leg linkages that are actuated by the leg endpoint units. The aforementioned units follow the sinusoidal grooves on the cylindrical cam by using a collection of roller cam-followers. The rotating cam, when rotated counterclockwise, generates axial contractive waves in the body segments, which are transformed into radial expansion and contraction of the leg linkages, which are shown in Fig. 6.

In comparison with biological peristaltic motion, which can be characterized by longitudinal and/or diametric deformations across the organism body, each body segment goes through two distinct phases during each locomotion stride. In the first phase, the diameter of the body segment legs increases while the axial distance between the leg endpoint units decreases simultaneously. The first phase corresponds to an earthworm longitudinal muscle contraction [17]. In the second phase, the diameter of the body segment legs decreases while the axial distance between the leg endpoint units increases simultaneously. The second phase corresponds to an earthworm circumferential muscle contraction [17].

A propulsive stroke of a body segment involves contracting the longitudinal (axial) distance between leg endpoint units, and extending the diameter made by the leg linkages. During a return stroke, the longitudinal distance between leg endpoint units is increased, and the diameter made by the leg linkages is contracted. When the robotic platform is partially submerged in granular media, the larger-diameter propulsive strokes would propel a greater amount of granular media than smaller-diameter return strokes. The robotic platform would therefore travel in the direction opposite that of the propulsive strokes. During the propulsive strokes of a body segment, the leg linkages are fully extended, and the longitudinal distance between the leg endpoint units is contracted. During the return strokes, the diameter of the leg linkages is contracted, and the leg endpoint units longitudinal distance is extended to their maximum.

In order to allow segments with larger diameter to act as anchors and minimize backsliding while the other segments are in their return stroke phase, we decided to sequentially actuate the axial position of each body segment from front to rear during the rotation of the cylindrical cam. In order to achieve this sequential contraction functionality, we grooved



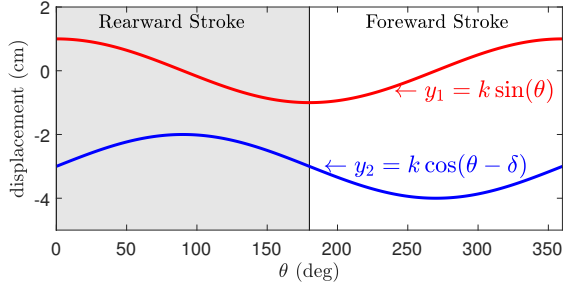


Fig. 7: Plot of the individual functions used to generate the axial motions of leg endpoint units in a single body segment: The component strokes in the gray and white backgrounds correspond to the rearward and forward propulsive strokes of the leg endpoint units during a single cam rotation, respectively.

pairs of phase-shifted sinusoids on the cam as the motion path for each cam-follower. Since the displacement functions of the developed cylindrical cam are sinusoidal, the first and second derivatives of these functions will also be continuous and sinusoidal. These profiles therefore abide by the fundamental law of cam design, which states that for any cam profile designed for operation other than at very low speeds, the cam-follower function needs to have a continuous velocity and acceleration, as well as a finite jerk [18].

With a phase shift of  $\delta$ , the physical motion of the robot legs due to the motion of the cam-followers on the phase-shifted sinusoids be described as follows (see also Fig. 7). During half of the period of the cam rotation, the legs perform a rearward-motion where there is a small distance between the curves (indicated with the gray background in Fig. 7). During the other half of the period, the rearward propulsive stroke is followed by a forward return stroke where there is an increased distance between  $y_1$  and  $y_2$  (indicated with the white background in Fig. 7). The difference between the rearward backsliding motion and the forward propulsive motion, which is due to the phase shifts between the sinusoidal grooves on the cam, is what causes the net forward motion of our peristaltic mechanism. The propulsive effect of phase shifts is also captured by the dynamical model derived in Section II (see (18)).

In our mechanism design, which has got three body segments, we have chosen the following grooved curve profiles

$$\phi_1(\theta) = k \cos(\theta), \quad (20a)$$

$$\phi_2(\theta) = k \cos(\theta - \delta_1), \quad (20b)$$

$$\phi_3(\theta) = k \cos(\theta - \delta_2), \quad (20c)$$

$$\phi_4(\theta) = k \cos(\theta - \delta_3), \quad (20d)$$

where the phase shifts between the sinusoidal grooves are chosen to be  $\delta_1 = 120^\circ$ ,  $\delta_2 = 240^\circ$ , and  $\delta_3 = 360^\circ$ , respectively. Furthermore,  $k$  is the amplitude of the sinusoidal curves. In our 0.8 inch diameter cylinder, the amplitude  $k$  has been set equal to  $1/4$  radians.

The cam groove sinusoidal profiles associated with the functions  $\phi_i(\theta)$  and  $\phi_{i+1}(\theta)$ ,  $i = 1, 2, 3$ , in (20), correspond to the movement of the  $i^{\text{th}}$  and the  $i + 1^{\text{th}}$  leg endpoint units. When the cylindrical cam rotates with frequency  $\omega$ , the angular position of the cam-followers on the grooves are determined by the angular position of the cam, i.e.,  $\theta = \omega t$ . Consequently, the vector  $\phi(\theta) = [\phi_1(\theta), \dots, \phi_4(\theta)]^T$ , where  $\theta = \omega t$ , corresponds to the driving input  $\phi_c(t, \delta)$  in (17).

### B. Cam-Follower Development

In our peristaltic robotic mechanism, roller cam-followers are used to transfer force from the cylindrical cam to each of the leg endpoint units with an small amount of internal friction (see the exploded view in Fig. 5). The reason for choosing roller cam-followers is that they generate a lower sum of sliding and rolling friction in comparison with sliding contact cam-followers [18].

Given the low speed of the robot motion, we have designed each of the leg linkages to operate without bearings. Furthermore, linkages are assembled by press-fitting aluminum pins through the outer elements of each joint (see Fig. 5). The middle element of each linkage joint is axially constrained on the pin between its outer elements and is free to rotate on the pin with a clearance fit.

Using a commercially Fused Deposition Modeling 3D-printer, the entire mechanism was largely 3D-printed from PLA. However, initial tests of the cylindrical cam made from the same printer proved unsatisfactory. This was due to the frequent shakes and complete system stalls that occurred as the cam-follower of the leg endpoint unit shafts dug into visibly distinct layers of PLA. Later cylindrical cam prototypes were printed from Nylon powder with a Selective Layer Sintering 3D printer, which resulted in noticeably smoother actuation of the leg linkages.

### C. Other design considerations

The system is driven by a 488:1-reduction Pololu gear-motor, which is constrained to the cylindrical cam by a setscrew. Motor control is limited to a voltage, which is set by a bench-top power supply. In our early prototype, no position or velocity control hardware were implemented. We found out that a major cause of system stalling is due to binding/twisting of guide rails that are attached to the sides of the robot. During the operation of the mechanism, torque is constantly transferred from the cylindrical cam, through the cam-followers, and into each of the leg endpoint units. The sum of these torques result in a twisting of the steel guide rails. If the rails twist significantly, the leg endpoint units will bind against the rails and will not be able to move axially across the cylindrical cam. We resolved the issue of guide rail binding/twisting by adding a collection of laser-cut acrylic plates with press-fit holes on both of the front and back ends of the robot. This solution constrains the guide rails to lie in a parallel formation.

Initial mobility tests in fine sand and dirt resulted in a large amount of material packing between linkages. To resolve this issue, we adhered a thin sheet of High Density Polyethylene

(HDPE) to the far ends of the underside of the robot. We decided to constrict the sheet at the far ends and the center two body segments with elastic straps to increase the variation in the diameter of the outer profile. This improvement significantly increases the amount of granular media, which are propelled rearwards during the robot operation. Finally, our robot platform can be powered by a commercial 9V battery while carrying the battery weight without issues.

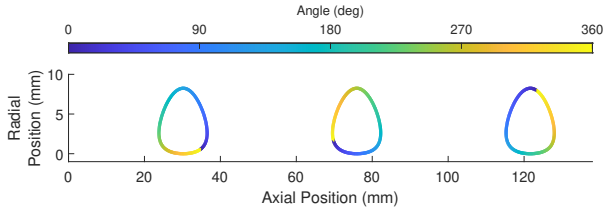


Fig. 8: Illustration of the leg tip positions during a full rotation of the cylindrical cam. In the figure, the radial position of 0 mm corresponds to the maximum leg extension, and the axial position of 0 mm corresponds to the front of the robot platform. In the figure, the leg tip motion is counterclockwise.

During the operation of the robot, we expect that the motor torque output would not be entirely converted into propulsive force on granular media, where the greatest efficiency losses would be due to imperfect propulsion of granular media in a direction opposite to that of the direction of the robot forward motion. Furthermore, the performance of the mechanism during both surface mobility testing and propulsive force testing is heavily influenced by the angle of repose, a characteristic of granular media, which is determined by the shape of the media particles, coefficients of friction, density, surface area, and the degree of water intrusion [19].

The motion of the tips of a set of legs is shown in Fig. 8. In this figure, the leg tips move counterclockwise, while having the most amount of engagement with the ground media during their maximum extension. As the leg tips continue to move along their motion paths, the legs will move in a negative axial direction. The legs of the robotic mechanism would not be in as much contact with the ground media during negative axial motion, in comparison with the full extension phase. However, an amount of ground media will inevitably be propelled in a direction opposite to the intended direction of robot platform motion. We refer to this reverse propulsion, and resultant negative displacement of the system as “backsliding”. The volume of media propelled during backsliding is dependent on both the depth of submersion of the robotic platform in granular media and the angle of repose of the granular media. The backsliding phenomenon is also captured by the dynamical model in Section II (see Fig. 4b).

#### IV. EXPERIMENTAL RESULTS

In this section, we present a series of surface mobility tests across a variety of terrains that consist of different granular material. In order to conduct the experiments, terrain media



Fig. 9: Overhead photo of the peristaltic robot in Martian Garden Coarse-Grade Basalt terrain media.

was arranged in wide 1.2 cm deep paths. For consistency, we lightly flattened the paths in a way to avoid overly compressing the terrain. Our selected granular material included a slightly wetted Kolorscape™ All Purpose Sand, Basalt crushings in Coarse, Fine and Super Fine grades of MMS-1<sup>1</sup>, and Assorted Soil that consisted of a non-homogenous mixture of topsoil, small rocks, and small pieces of wood. Using the fixed funnel method [20], we calculated the average of five measurements of the static angles of repose associated with each granular media. In order to compute the angles of repose, we created roughly-conical material piles and found the angle of repose by calculating the arctangent of the material pile height divided by the radius of the cone.

In order to record the movement of our mechanism, Vicon tracking markers were affixed to the front and rear ends of the mechanism as well as to each individual leg as shown in Fig. 9. We utilized a Vicon real-time motion tracking system to track the displacement of the mechanism over time on each surface over a distance of 180 mm. In order to improve line-of-sight tracking of the Vicon markers, two rows of legs were removed during the experiments. The DC motor was run at 11 volts during all trials, resulting in a full rotation of the cylindrical cam roughly every 2.3 seconds. Snapshots of the robotic mechanism locomotion while traversing the All Purpose Sand media are depicted in Fig. 10.

Figure 11 depicts the average forward displacement of the two front tracking balls, which are indicated with the red circles in Fig. 9. As it is predicted in Section II, changing the direction of rotation of the axial cam induces motion in an opposite direction. The green rectangular area denotes a single rotation of the cylindrical cam, as detailed in the inset. As shown in the inset in Fig 11, the backsliding phenomenon is clearly observed as our derived dynamic model has captured. On each tested terrain, the robot has a roughly consistent backsliding behavior during each rotational cycle of the cylindrical cam. As seen in Fig. 11, backsliding occupies roughly one-third of the time of the rotational cycle. The ratio of a rotational cycle’s displacement during backsliding to forward displacement varies greatly between tested terrains. It is remarked that the numerical simulation results, which are depicted in Fig. 4, have very close resemblance to the actual experimental results depicted in Fig. 11.

As shown in Fig. 11 and Table 1, the highest speed of the robotic mechanism was achieved on All-Purpose Sand.

<sup>1</sup> [www.themartiangarden.com](http://www.themartiangarden.com)

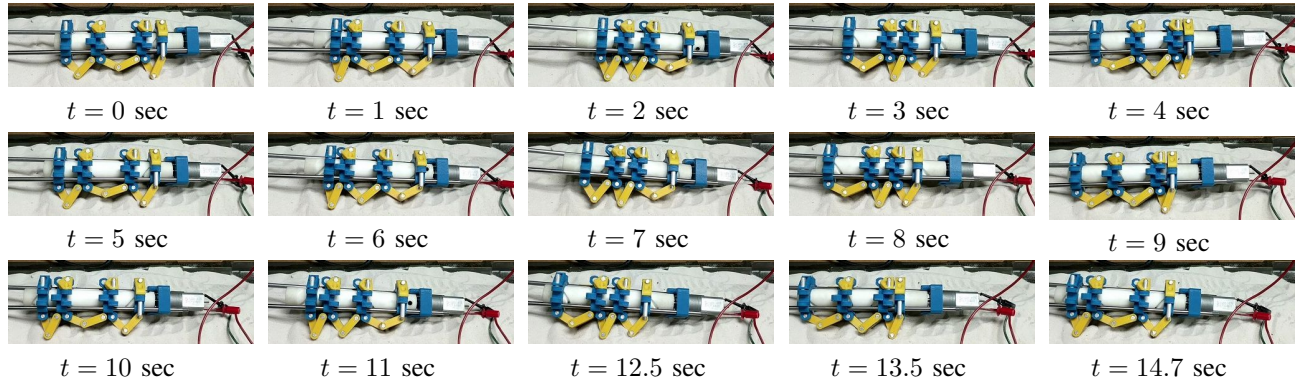


Fig. 10: Snapshots of the robotic mechanism locomotion.

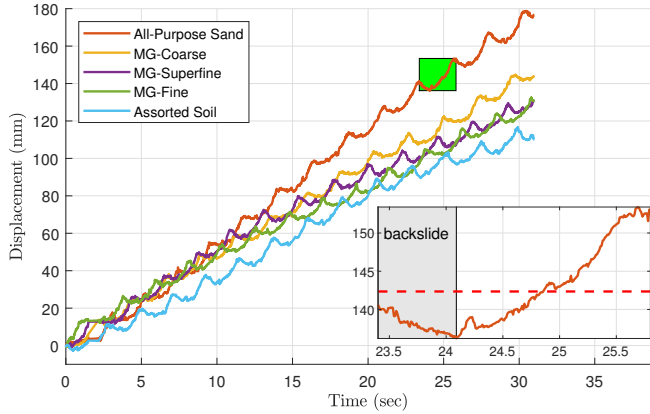


Fig. 11: Displacement over time in five mobility trials. The green rectangular area denotes the peristaltic motion of the robot during a single rotation of the cylindrical cam, which is plotted in the inset. The segment of the locomotion stride in which the mechanism backslides is indicated via the gray background. The dashed red line corresponds to the average displacement of the mechanism in one stride.

This terrain tied with Coarse Basalt for the smallest recorded average backslide length. A larger average backslide length does not appear to necessarily correlate with a faster robot velocity. The average backslide displacement in the grades of Basalt does correlate with the fineness of the media, with the smallest backslides on Coarse and the largest backslides on Super Fine. However, these do not appear to directly correlate with the robot's speed. While the highest speed correlated with the highest material angle of repose, on All-Purpose Sand, the other angle of repose measurements do not appear to significantly correlate with the other media.

Lastly, we took propulsive force measurements on each granular media, and running the mechanism until forward progress ceased. These results are noted in Table 2. The material angle of repose roughly correlates with the measured forward propulsive force.

Figure 12 depicts the measurements of induced electrical power when an 11V DC voltage was applied to the robot. When the robot was operated in the air (i.e., no external load was applied to the robot), the average induced power

TABLE I: Comparison of robot platform speed and backsliding severity on various types of granular media. The angle of repose ( $\theta$ ) of the media is compared with the speed of the robotic mechanism, or the slope of the linear curve-fit ( $v$ ), the average of 5 backsliding events ( $b$ ), and Force generated ( $f$ ).

Granular Media	$\theta$ (deg)	$v$ (mm/s)	$b$ (mm)	$f$ (N)
All-Purp. Sand	45.32	6.03	3.47	2.45
Coarse Basalt	35.30	4.71	3.47	2.17
Fine Basalt	32.06	3.91	4.01	1.23
S-Fine Basalt	33.83	4.11	5.75	1.57
Assorted Soil	35.53	3.99	4.62	1.67

was 0.83 W. When the robot was moving on All-Purpose Sand, its forward propulsive force was the largest among the tested mediums, the induced power was 1.14 W, which is also the greatest. The power consumption on the other tested mediums fell into the range of 1.03-1.08 W. With a 9 V household battery with the battery capacity of 500 mAh, the robot can be operated more than half an hour.

## V. CONCLUSION AND FUTURE WORK

In this paper, we design a novel mechanism to generate peristaltic waves on the exterior of robotic systems. Our method provides a scalable mechanism for both on-terrain and potentially submerged locomotion in granular media. Through testing, the cylindrical cam-actuated Sarrus Linkage mechanism has shown to be capable of traveling up to 6 mm/sec atop a  $51^\circ$  angle of repose medium, and generate up to 2.45 N of forward propulsive force.

Future work will consist of design optimization for not only surface operation, but for effective submerged digging. Efforts will need to be made in order to reduce the severity of backsliding events, such as optimizing the leg linkage topology or using specialized cylindrical cam groove patterns for granular media for various ranges of angle of repose. Initial studies into fully submerged digging compressed the granular media ahead of the robot, as opposed to moving the media out of the path of travel. The compaction issue may be resolved by implementing a head module consisting of proven devices such as a conventional spinning augur/drill [21],



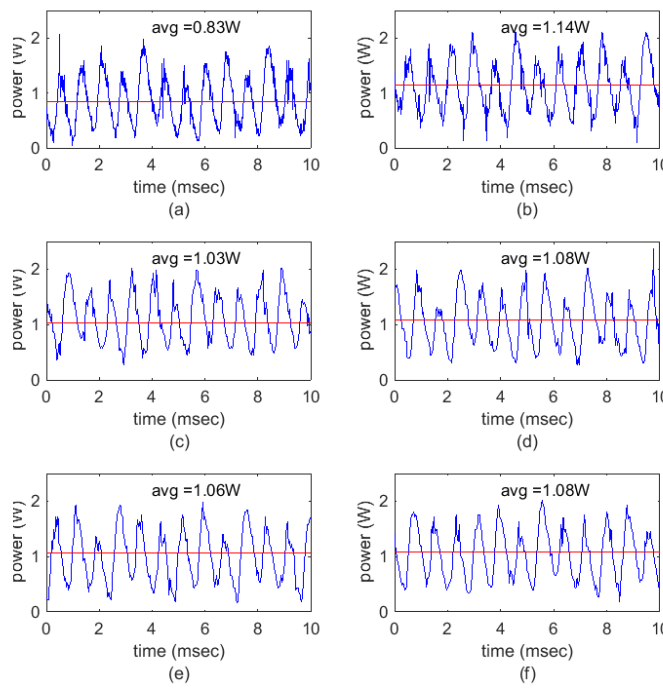


Fig. 12: Power measurements of the robot on various terrains. (a) In air (0.83W); (b) on all-purpose sand (1.14W); (c) Coarse Basalt (1.03W); (d) Fine Basalt (1.08W); (e) Superfine Basalt (1.06W); (f) Assorted Soil (1.08W). The red lines in the plots indicate the average consumed power over a 10 sec interval.

[22], oscillating hammer [23], [24], or a hammer drill [25]. Additional efforts may investigate direction control using methods similar to the ones proposed by Liljebäck *et al.* [26].

## REFERENCES

- [1] H. Otori, T. Murakami, H. Nagai, T. Nakamura, and T. Kubota, "Development of a novel bio-inspired planetary subsurface explorer: Initial experimental study by prototype excavator with propulsion and excavation units," *IEEE/ASME Transactions on Mechatronics*, vol. 18, no. 2, pp. 459–470, 2013.
- [2] K. Wang, G. Yan, P. Jiang, and D. Ye, "A wireless robotic endoscope for gastrointestinal," *IEEE Transactions on Robotics*, vol. 24, no. 1, pp. 206–210, 2008.
- [3] A. Kohl, E. Kelasidi, A. Mohammadi, M. Maggiore, and K. Pettersen, "Planar maneuvering control of underwater snake robots using virtual holonomic constraints," *Bioinspiration & Biomimetics*, vol. 11, no. 6, p. 065005, 2016.
- [4] E. Kelasidi, K. Y. Pettersen, P. Liljebäck, and J. T. Gravdahl, "Integral line-of-sight for path following of underwater snake robots," in *Proceedings of IEEE Conference on Control Applications (CCA)*. IEEE, 2014, pp. 1078–1085.
- [5] J. M. Hefferman and S. A. Wainwright, "Locomotion of the holothurian *Euplota lappa* and redefinition of peristalsis. Biol. Bull." *The Biological Bulletin*, vol. 147, no. 1, pp. 95–104, 1974.
- [6] J. Gao and G. Yan, "Locomotion analysis of an inchworm-like capsule robot in the intestinal tract," *IEEE Transactions on Biomedical Engineering*, vol. 63, no. 2, pp. 300–310, 2016.
- [7] A. Di Lallo, M. Catalano, M. Garabini, G. Grioli, M. Gabiccini, and A. Bicchi, "A novel approach to under-actuated control of fluidic systems," in *2018 IEEE International Conference on Robotics and Automation (ICRA)*, 2018, pp. 193–199.
- [8] Y. Tanaka, K. Ito, T. Nakagaki, and R. Kobayashi, "Mechanics of peristaltic locomotion and role of anchoring," *Journal of the Royal Society Interface*, vol. 9, no. 67, pp. 222–233, 2011.
- [9] K. J. Quillin, "Kinematic scaling of locomotion by hydrostatic animals: ontogeny of peristaltic crawling by the earthworm *lumbricus terrestris*," *Journal of Experimental Biology*, vol. 202, no. 6, pp. 661–674, 1999.
- [10] C. Gardner, "The neuronal control of locomotion in the earthworm," *Biological Reviews*, vol. 51, no. 1, pp. 25–52, 1976.
- [11] T. Nakamura and T. Iwanaga, "Locomotion strategy for a peristaltic crawling robot in a 2-dimensional space," in *Proceedings of IEEE International Conference on Robotics and Automation*, 2008, pp. 238–243.
- [12] S. Niu, Y. Luo, Y. Shen, and K. J. Kim, "Enabling earthworm-like soft robot development using bioinspired IPMC-scissor lift actuation structures: Design, locomotion simulation and experimental validation," in *Proceedings of IEEE International Conference on Robotics and Biomimetics*, 2015, pp. 499–504.
- [13] A. S. Boxerbaum, H. J. Chiel, and R. D. Quinn, "A new theory and methods for creating peristaltic motion in a robotic platform," in *Proceedings of IEEE International Conference on Robotics and Automation*, 2010, pp. 1221–1227.
- [14] E. Rezapour, A. Hofmann, K. Y. Pettersen, A. Mohammadi, and M. Maggiore, "Virtual holonomic constraint based direction following control of planar snake robots described by a simplified model," in *Proceedings of IEEE Conference on Control Applications (CCA)*, 2014, pp. 1064–1071.
- [15] P. Liljebäck, K. Y. Pettersen, Ø. Stavdahl, and J. T. Gravdahl, "A simplified model of planar snake robot locomotion," in *Proceedings of IEEE International Conference on Intelligent Robots and Systems (IROS)*, 2010, pp. 2868–2875.
- [16] K. Hunt, "Prismatic pairs in spatial linkages," *Journal of Mechanisms*, vol. 2, no. 2, pp. 213–230, 1967.
- [17] K. J. Quillin, "Kinematic scaling of locomotion by hydrostatic animals: ontogeny of peristaltic crawling by the earthworm *lumbricus terrestris*," *The Journal of experimental biology*, vol. 202, no. 1999, pp. 661–74, 1999.
- [18] R. L. Norton, *Design of Machinery*, 4th ed. McGraw-Hill Science, 2003, vol. 125, no. 3.
- [19] A. Mehta and G. C. Barker, "The dynamics of sand," *Reports on Progress in Physics*, vol. 57, no. 4, pp. 383–416, apr 1994.
- [20] H. M. Beakawi Al-Hashemi and O. S. Baghabra Al-Amoudi, "A review on the angle of repose of granular materials," *Powder Technology*, vol. 330, pp. 397–417, 2018.
- [21] T. M. Myrick and S. Gorevan, "Self-propelled instrumented deep drilling system," US005485919A, Tech. Rep., 2006.
- [22] K. Nagaoka, T. Kubota, M. Otsuki, and S. Tanaka, "Robotic screw explorer for lunar subsurface investigation: Dynamics modelling and experimental validation," in *Proceedings of International Conference on Advanced Robotics*, 2009.
- [23] T. Spohn, M. Grott, S. E. Smrekar, J. Knollenberg, T. L. Hudson, C. Krause, N. Müller, J. Jänchen, A. Börner, T. Wippermann, O. Krömer, R. Lichtenheldt, L. Wisniewski, J. Grygorczuk, M. Fittock, S. Rheershemius, T. Spröwitz, E. Kopp, I. Walter, A. C. Plesa, D. Breuer, P. Morgan, and W. B. Banerdt, "The heat flow and physical properties package (HP<sup>3</sup>) for the insight mission," *Space Science Reviews*, vol. 214, no. 5, p. 96, Aug 2018.
- [24] C. R. Stoker, A. Gonzales, and J. R. Zavaleta, "The Mars and Moon underground mole," in *Proceedings of NASA Technology and Science Conference*, June 2007.
- [25] K. Zacny, G. Paulsen, Y. Bar-Cohen, L. Beegle, S. Sherit, M. Badescu, B. Mellerowicz, O. Rzepiejewska, J. Craft, S. Sadick, F. Corsetti, Y. Ibarra, X. Bao, Hyeong Jae Lee, and B. Abbey, "Wireline deep drill for exploration of mars, europa, and enceladus," in *2013 IEEE Aerospace Conference*, March 2013, pp. 1–14.
- [26] P. Liljebäck, I. U. Haugstuen, and K. Y. Pettersen, "Path following control of planar snake robots using a cascaded approach," *IEEE Transactions on Control Systems Technology*, vol. 20, no. 1, pp. 111–126, Jan 2012.